Published in final edited form as:
Mol Imaging Biol. 2012 October ; 14(5): 584–592. doi:10.1007/s11307-011-0534-y.

In Vivo Quantification of Tumor Receptor Binding Potential with Dual-Reporter Molecular Imaging

Kenneth M. Tichauer[1], **Kimberley S. Samkoe**[1,2], **Kristian J. Sexton**[1], **Shannon K. Hextrum**[1], **Harold H. Yang**[1], **W. Spencer Klubben**[1], **Jason R. Gunn**[1], **Tayyaba Hasan**[3], and **Brian W. Pogue**[1,2,3]

[1]Thayer School of Engineering, Dartmouth College, Hanover, NH, 03755, USA

[2]Department of Surgery, Dartmouth Medical School, Lebanon, NH, 03756, USA

[3]Wellman Center for Photomedicine, Massachusetts General Hospital, Boston, MA, 02114, USA

Abstract

Purpose—Receptor availability represents a key component of current cancer management. However, no approaches have been adopted to do this clinically, and the current standard of care is invasive tissue biopsy. A dual-reporter methodology capable of quantifying available receptor binding potential of tumors *in vivo* within a clinically relevant time scale is presented.

Procedures—To test the methodology, a fluorescence imaging-based adaptation was validated against *ex vivo* and *in vitro* measures of epidermal growth factor receptor (EGFR) binding potential in four tumor lines in mice, each line expected to express a different level of EGFR.

Results—A strong correlation was observed between *in vivo* and *ex vivo* measures of binding potential for all tumor lines (r=0.99, p<0.01, slope=1.80±0.48, and intercept=−0.58±0.84) and between *in vivo* and *in vitro* for the three lines expressing the least amount of EGFR (r=0.99, p<0.01, slope=0.64±0.32, and intercept=0.47±0.51).

Conclusions—By providing a fast and robust measure of receptor density in tumors, the presented methodology has powerful implications for improving choices in cancer intervention, evaluation, and monitoring, and can be scaled to the clinic with an imaging modality like SPECT.

Keywords

Molecular imaging; Fluorescence; Targeted reporter; Epidermal growth factor receptor; Mouse model

Introduction

The recent widespread application of novel molecular cancer therapies has made the monitoring of tumor receptor status an important component of current cancer management. However, no clinically feasible approaches have yet to be adopted to do this *in vivo*, and tissue biopsy has been required. Molecular imaging has become a valuable tool for locating tumors *in vivo* in both preclinical and clinical cancer research and diagnosis. It also has the potential to measure the expression of specific molecular and biological processes that influence tumor behavior or affect response to therapies. In this study, the methodology and

Correspondence to: Kenneth Tichauer; Kenneth.Tichauer@dartmouth. edu, Brian Pogue; Brian.W.Pogue@dartmouth.edu.

Conflicts of interest. The authors have no conflicts of interest.

a validation of a molecular imaging approach capable of quantifying *in vivo* available receptor density in tumors in a clinically feasible time frame that does not require blood sampling is presented. This ability has the potential to provide an earlier detection marker of cancer, stratification of patients for specific treatments, and/or the ability to evaluate the efficacy of new therapies on a patient-by-patient basis [1].

The challenge in quantifying receptor expression *in vivo* stems from the fact that tissue uptake of a targeted imaging reporter is dependent on many factors. Two major factors that confound receptor quantification in cancer include a variable delivery rate of the reporter to the tissue (owing to regional variations in hemodynamics) and non-specific uptake of the reporter in the tissue, *e.g.*, by the enhanced permeability and retention (EPR) effect in tumors [2]. Activatable fluorescent reporters have been used in an attempt to partially mitigate these complications [3, 4]; however, their uptake is still dependent on hemodynamic delivery of the reporter, and while this approach does provide information on the amount of reporter binding, it cannot be used to determine receptor expression. Another approach of quantifying receptor expression in tumors has been investigated that avoids blood sampling by modeling the shape of the plasma input from the uptake of a targeted reporter at early time points [5]; however, at this time, the time-scale required for this approach is not clinically feasible.

Brain neurotransmitter positron emission tomography (PET) studies have addressed the delivery problem by either directly taking arterial blood samples [6] or using the uptake of the reporter in a tissue region void of specific receptor ("reference tissue") as a surrogate of the arterial input function [7, 8]. Unfortunately, two problems arise when attempting to apply these approaches to a broader range of organs and pathologies. One problem is that it may not be possible to find a reference tissue that satisfies all the requirements of the reference tissue model, *i.e.*, that the tissue be void of receptors and have similar vascular permeability and non-specific uptake to the region of interest [7]. Another problem is that even if invasive blood samples are acquired, the arterial input alone cannot account for nonspecific uptake of a reporter. These issues become particularly problematic when applied to cancer imaging since tumors often have quite irregular hemodynamics [9], leaky vasculature, and ineffective lymphatic drainage that lead to substantial non-receptor-mediated uptake and retention of a reporter [10].

In response, a new approach that overcomes the two major quantification issues by simultaneously injecting an untargeted reporter with the targeted reporter was developed [11–14]. In this scenario, it is possible to replace the "reference tissue" input used in PET with the uptake of the untargeted reporter. In fact, the untargeted reporter uptake is an improvement over the reference tissue input because the uptake of the untargeted reporter is from the same tissue as the uptake of the targeted reporter. As such, it experiences the same hemodynamics, vascular permeability, and level of non-specific uptake as the targeted reporter. Essentially, the approach builds on the dual-tracer approach pioneered by Goldenberg *et al.* [11] and Hine *et al.* [12] for improving cancer detection with single photon emission tomography (SPECT) of radiolabeled antibodies in 1980 and incorporates the sophistication of the neurotransmitter PET models [7, 8] to accurately quantify receptor binding potential.

To demonstrate the feasibility of this dual-reporter approach to quantifying receptor expression, a study employing two near-infrared fluorescent reporters that emitted light at different wavelengths was carried out. One reporter (the targeted reporter) was bound to human epidermal growth factor (EGF) to target and image EGF receptor (EGFR) expression (a receptor overexpressed in many cancer lines). The second reporter was left unbound (untargeted reporter) and was mixed in equal concentrations with the targeted reporter. The

uptake of the two reporters was then imaged with a near-infrared fluorescence scanner for 1 h following a tail vein injection of the reporter mixture into immunodeficient mice. The mice were implanted with one of four different tumor lines: human epidermoid carcinoma A431, known to express very high levels of EGFR; human pancreatic adenocarcinoma AsPC-1 and human neuronal glioblastoma U251, known to express moderate levels of EGFR; and a green fluorescent protein (GFP) expressing rat gliosarcoma 9L-GFP, not expressing human EGFR. The *in vivo* receptor density of EGFR was quantified in all tumor groups using the dual-reporter approach, and the results were validated against expected receptor density determined *ex vivo* and *in vitro*.

Methods

Dual-Reporter Model

The distribution of both the targeted and untargeted reporters was modeled on the simplified solution to the two-tissue compartment reference tissue model introduced by Lammertsma *et al.* [7] and Logan *et al.* [8] in 1996. More specifically, the concentration of the targeted reporter in a region of interest was modeled as a sum of the concentration of the reporter in the blood and in two tissue compartments: the blood plasma concentration, C_p; the unbound and/or non-specifically bound concentration in the interstitial space, C_f; and the concentration of reporter attached to its specific receptor, C_b. Then, the concentration of the untargeted reporter was modeled as a sum of the same blood plasma concentration, C_p, and the unbound and/or non-specifically bound concentration of the untargeted reporter in the interstitial space, C_r, which could be different from the corresponding compartment of the targeted reporter, C_f. These relationships can also be expressed by the following equations:

$$\mathrm{ROI}_{\mathrm{T}}(t)=C_p(t)+C_f(t)+C_b(t) \quad \text{and} \quad (1)$$

$$\mathrm{ROI}_{\mathrm{UT}}(t)=C_p(t)+C_r(t), \quad (2)$$

where $\mathrm{ROI}_{\mathrm{T}}(t)$ and $\mathrm{ROI}_{\mathrm{UT}}(t)$ are the measured region of interest concentrations of the targeted and untargeted reporters, respectively, as a function of time, t. Note that C_p is defined as the concentration of reporter in a region of interest, divided by the volume of the region of interest. Since C_p is never actually measured in this study, it is not essential then to involve the blood volume or other compartmental volumes. The exchange rates of reporter populations were then modeled between the different compartments (Fig. 1c) on first-order kinetics using the following set of differential equations:

$$\frac{dC_f}{dt}=K_1C_p(t)-(k_2+k_3)C_f(t)+k_4C_b(t), \quad (3)$$

$$\frac{dC_b}{dt}=k_3C_f(t)-k_4C_b(t), \text{ and} \quad (4)$$

$$\frac{dC_r}{dt}=K_1^{'}C_p(t)-k_2^{'}C_r(t), \quad (5)$$

where K_1 is the rate constant governing the extraction of either reporter from the plasma into the interstitial compartment, k_2 is the rate constant governing the leakage of reporter out of the interstitial space back into the plasma, k_3 is the rate constant governing the binding of reporter in the interstitial space to specific receptors, and k_4 is the rate constant governing the separation of the bound reporter from its specific receptor back into the interstitial space.

K_1 is intentionally capitalized to indicate that it is the only rate constant that is dependent on the blood flow in the region of interest. The prime indices on K_1 and k_2 in Eq. 5 indicate that the rate constants of the non-targeted reporter may be different from those of the targeted reporter.

Lammertsma *et al.* [7] solved Eqs. 3, 4, and 5 by assuming that C_f and C_b are in an instantaneous equilibrium with each other (*i.e.*, the system can be modeled as an adiabatic process) and that the ratio of K_1 over k_2 is equal to the ratio of K_1' over k_2'. If the same assumptions are made for the current model and it is further assumed that C_p for the targeted and untargeted reporters is roughly equivalent (demonstrated by Samkoe *et al.* [15]), the same solution reached by Lammertsma *et al.* can be applied to the current model as follows:

$$\mathrm{ROI_T}(t)=R_1\mathrm{ROI_{UT}}(t)+\left\{k_2-\frac{R_1k_2}{1+\mathrm{BP_{ND}}}\right\}\mathrm{ROI_{UT}}(t)*e^{-\frac{k_2t}{1+\mathrm{BP}}}, \quad (6)$$

where R_1 is equal to K_1/K_1', * represents the convolution operator, and $\mathrm{BP_{ND}}$ is exactly equal to k_3/k_4 and is termed the "non-displaceable binding potential" ($\mathrm{BP_{ND}}$) because it is equal to the product of the affinity of the targeted reporter for its receptor and the receptor density [16]. The dependence of $\mathrm{BP_{ND}}$ on the receptor density makes it the key parameter of interest in this study.

Similarly, the Logan graphical reference tissue approach [8] can be adapted to the dual-reporter model where the equation:

$$\frac{\int_0^t \mathrm{ROI_T}(u)du}{\mathrm{ROI_T}(t)}=(\mathrm{BP_{ND}}+1)\frac{\int_0^t \mathrm{ROI_{UT}}(u)du}{\mathrm{ROI_T}(t)}+\mathrm{int}' \quad (7)$$

is a linear relationship between two measurable ratios with a slope equivalent to the binding potential plus one. The last term of Eq. 7, int′, becomes constant at some time, $t'>t$, when steady state has been reached (u is a dummy time variable).

Animal experiments

The accuracy of the proposed dual-reporter model was investigated in 27 6-week-old severe combined immunodeficient (SCID) male mice (Charles River, Wilmington, MA, USA). The mice were randomly separated into four separate groups. The first group (n=6) were inoculated with human epidermoid carcinoma (A431; ATCC, Manassas, VA, USA) subcutaneously in the outside of the left leg. The mice in the second group (n=6) were inoculated with a human pancreatic adenocarcinoma (AsPC-1; from author T. Hasan) orthotopically using a method described elsewhere [17]. The mice in the third group (n=9: n=6 for the targeted study and n=3 for the blocking control study) were inoculated with a human neuronal glioblastoma (U251; from Dr. Israel at Dartmouth College) subcutaneously in the left outer thigh. The mice in the final group (n=6) were inoculated with a rat gliosarcoma (9L-GFP; from Dr. Bogdanov at Dartmouth College), also subcutaneously in the outer left thigh. All cell lines were tested annually for murine pathogens. These four tumor lines were chosen because they are each expected to express differing levels of EGFR. A431 is known to express a very large amount of EGFR [18], while 9L-GFP is known to express very little [19]. AsPC-1 and U251 were expected to express moderate levels of EGFR [19, 20]. Tumors were allowed to grow to a size of approximately 150 mm^3 before imaging. Just prior to imaging, the mice were anesthetized with an intra-peritoneal injection of ketamine–xylazine (100 mg/kg:10 mg/kg i.p.), and the superficial tissue surrounding the tumors was removed. In three U251 mice, a 30-nmol (100 ml PBS)

intravenous injection of free human recombinant EGF (Millipore, Temecula, CA, USA) was administered 1 h prior to imaging session to carry out a blocking study (negative control). The mice were then placed tumor-side down on a glass slide and loosely secured with surgical tape (Fig. 1f). Once plated, the mice were positioned in an Odyssey Scanner (LI-COR Biosciences, Lincoln, NE, USA). The Odyssey Scanner employs raster scanning and two lasers, one at 685 nm and another at 785 nm, to excite the fluorophores pixel-by-pixel, utilizing a series of dichroic mirrors to decouple epi-illumination collected fluorescence from the LI-COR 700 nm fluorescent reporter and the LI-COR 800 nm fluorescent reporter.

The scanning procedure included collecting a pre-injection scan to determine background fluorescence followed by a tail vein injection of 1 nmol of an EGFR-targeted reporter (IRDye 800CW EGF; LI-COR Biosciences, Lincoln, NE, USA) mixed with 1 nmol of a non-targeted reporter (carboxylate form of the IRDye 700DX NHS Ester; LI-COR Biosciences, Lincoln, NE, USA). The carboxylate form of the IRDye 700DX dye was created by reacting IRDye 700DX NHS ester in water (pH 8.5) for 4–5 h at room temperature as per instructions from the manufacture. This procedure left no residual IRDye 700DX in the NHS ester form. Scans were repeated every 90 s up to 20 min and then at intervals of approximately 5 min up to 1 h post-injection. Following the scans, the mice were sacrificed, and the tumors were excised for histology. The ratio of measured fluorescence from the targeted and untargeted reporters at all time points were normalized to ratio of fluorescence measured using the Odyssey system from a sample of the injected reporter solution. For each tumor line and for leg tissue, the average BP_{ND} of the targeted reporter was measured using the Lammertsma form of our dual-reporter model in each mouse. The curves used in this case were acquired by averaging targeted and untargeted reporter fluorescence at each time point from a region of interest over the area of the tumor that was in contact with the slide (determined from a white-light image) and from comparable region of interest on the exposed leg muscle. Alternately, the maps depicted in the main body of the article were produced using the Logan form of our dual-reporter model because it was found to be more resilient to noise (a basis function approach can also be employed for such a case [21]). A strong correlation between results obtained with each form of our model in low noise conditions and average binding potentials in the regions of interest mentioned above that were taken from the Logan-based maps matched well with the Lammertsma-based curve fitting results.

Binding potential validation (ex vivo)

An approximation of the BP_{ND} for a single time point measurement was developed by taking the ratio of Eqs. 1 and 2. It can be shown that this ratio is equivalent to $BP_{ND}+1$ if the following assumptions are made: (1) that the fraction of reporter signal coming from the plasma compartment is negligible, (2) that C_f and C_r are equivalent, and (4) that C_f and C_b are in an instantaneous equilibrium. BP_{ND} was measured using this approach on 10-μm-thick slices of excised tumor in the mouse study. Nine slices from every tumor were imaged on the Odyssey scanner, and the quotient of the targeted (800 nm) fluorescence image and the untargeted (700 nm) fluorescence image was taken and subtracted by one to produce a BP_{ND} map, from which the average *ex vivo* BP_{ND} was determined for all tumors.

Binding potential validation (in vitro)

The *in vitro* BP_{ND} measure used to validate the *in vivo* BP_{ND} was based on solving the following expression [16]:

$$BP_{ND} = k_A \cdot B_{avail}, \quad (8)$$

where k_A is the affinity of the reporter for the receptor (approximately 1×10^9 mole^{-1} for EGF and EFGR [22], and B_{avail} is the concentration of receptors *available* for binding in a given tissue. The parameter, $B_{avail}$was estimated by taking the product of the average number of receptors in each cell (determined by flow cytometry) and the average density of cells in a tissue (determined by histology).

Histology

Following each experiment, the tumor tissue was removed from the mouse, submerged in TissueTek® Optimum Cutting Temperature Medium (Sakura Finetek USA Inc., Torrance, CA, USA), and flash-frozen using a mixture of dry ice and methylbutane. The tissues were stored at −20°C (short term) or −80°C (long term) until sectioning. The frozen tissues were then cut into 10-μm sections using a Leica 1850M cryostat and stained with the fluorescent stain, 4′,6-diamidino-2-phenylindole (DAPI) dissolved in slide mounting medium (ProLong® Gold Antifade reagent with DAPI, Invitrogen, Camarillo, CA, USA) to identify individual cell nuclei. Fluorescent images were taken on a microscope (Olympus BX51 microscope fitted with a Q-Color3 CCD camera and a specialized DAPI filter U-MF2, Chroma, Bellows Falls, VT, USA) of ten regions in each tumor at a ×10 magnification and using identical camera settings. The software package, ImageJ (National Institutes of Health, Bethesda, MA, USA), was then used to translate each image into a binary mask by thresholding to create a black and white image, where black was cell nuclei and white was background. These masks were analyzed with ImageJ to determine the average *in vivo* cell density of each tumor line. More specifically, the cell density was calculated by determining area of DAPI staining in each image and dividing that by the median nucleus size while normalizing to the dimensions of the slice (surface area of 0.27 mm^2 and a slice thickness of 10 μm).

Flow cytometry

The number of receptors per cell was quantified for A431, AsPC-1, U251, and 9L-GFP using flow cytometry. When cells reached a confluence of 80%, they were trypsinized, counted, and washed with PBS. Each set of cells (5×10^5 cells) was then labeled with 4 μg/ml of EGF Biotin (Molecular Probes, Invitrogen, Camarillo, CA, USA), washed and secondarily labeled with a 1:25 dilution of Cy5-Streptavidin (Invitrogen, Camarillo, CA, USA). This process was repeated in triplicate for each tumor line and for control cells, which were stained only with the 1:25 dilution of Cy5-Streptavidin to account for autofluorescence and non-specific staining. Flow cytometric data was acquired with a FACSCalibur analysis system equipped with a FACStation, MAC PowerPC computer, and Cell Quest Acquisition software (Becton Dickinson, San Jose, CA, USA). The results were then compared to Quantum Cy5 MESF beads as described by the manufacturer (Bangs Laboratory, Fishers, IN, USA). Briefly, the blank Quantum Cy5 MESF beads were analyzed first to determine optimal flow rate, concentration, and the appropriate analysis gate. A standard concentration curve was then produced using supplied software (QuickCal v2.3, Bangs Laboratory) from the average fluorescence of the blank and fluorescent bead mixtures. Next, the resultant average fluorescence measured for the control cells was subtracted from the EGF stained cells to remove effects of autofluorescence and non-specific staining. Finally, the number of receptors per cell was calculated assuming one molecule of biotin per EGF and three Cy5 fluorophores per streptavidin molecule, as specified by Invitrogen.

Statistical analysis

All statistics in this study were carried out with the statistical package SPSS (IBM®, Armonk, NY, USA). A one-way ANOVA with Bonferroni correction was used, with the tumor-line as a between-subjects factor, to compare binding potentials in each group. A

linear regression was employed to compare *in vivo* with *in vitro* and *ex vivo* binding potentials. Statistical significance was based on $p<0.05$. All data are presented as mean±SD.

Results and Discussion

A white-light image and fluorescence uptake images of the targeted and untargeted imaging reporters at 60 min after injection are presented in Fig. 1a–c, respectively, for a subcutaneous U251 tumor. The white-light image displays the typical morphology of the subcutaneously grown tumors, exposed and ready for imaging. The false colored images in Fig. 1b, c demonstrate the quality of the typical fluorescence maps acquired at 700 and 800 nm wavelengths, respectively, in the Odyssey system at each imaging time point. Typical fluorescence uptake curves of targeted and untargeted reporter in a tumor region of interest, and the dual-reporter model fits, are depicted for all tumor lines in Fig. 2. There were clear differences between the uptake curves in different tumor lines, with a proportionately greater separation between targeted and untargeted reporter uptake observed for tumor lines expected to express more EGFR.

Additional fluorescence images of the uptake of untargeted and targeted reporter at 60 min post-reporter injection in all tumor lines are presented in the first two columns of Fig. 3, respectively. The average fluorescence contrast-to-background ratios (CBR) for the targeted reporter of the various tumors were generally quite low: 0.33±0.44, 3.35± 4.32, 1.60±1.95, 1.03±1.28, and 0.50±0.65 for the A431, AsPC-1, U251, 9L-GFP, and blocked U251 groups, respectively (this can be visualized in Fig. 4b). The low contrast observed suggests that much of the fluorescence uptake at early time points is non-specific-uptake related and not binding related (this is reflected in the similarities in the uptake maps of the targeted and untargeted reporters), and the large variance in CBR values within groups was likely related to inter-subject variability in tumor blood supply. Despite the low CBR observed for all tumor lines, the trend of fluorescence did match the expected EGFR expression levels of the various tumors except for the A431 tumor, which demonstrated very low fluorescence uptake. It is possible that the uptake was so low because of a high compressibility of the tumors, which may have caused a constricted blood flow to these tumors, since the animals were imaged tumor side down. However, Aerts *et al.* also observed a low uptake of targeted reporter in the A431 line in an imaging setup that did not have the potential to restrict blood supply [23], suggesting that the tumor has an inherently poor blood supply.

Corresponding *in vivo* binding potential maps are presented in the third column of Fig. 3. In these maps, the Logan-based dual-reporter model was employed on a pixel-by-pixel basis to demonstrate the differences in binding potential throughout the imaging field. The more accurate, yet less robust-to-noise, Lammertsma-based dual-reporter model was used to calculate the average non-displaceable binding potential (BP_{ND})—a product of target affinity and receptor expression [16]—from the uptake curves in all tumors (Fig. 2 presents typical fits of the model to the data). The average BP_{ND} in each tumor group were significantly greater than that of the control leg tissue ($p<0.05$). Furthermore, average BP_{ND} measures between tumor groups were statistically significant from each other ($p<0.05$), with the exception of A431 and AsPC-1. The trend in BP_{ND} matched the predicted trend in EGFR expression, where A431 demonstrated the highest BP_{ND}9L-GFP the lowest, and AsPC-1 and U251 in between. Furthermore, the lowest BP_{ND} was observed in the blocked U251 tumors and the leg muscles (tissue with no expected appreciable levels of EGFR expression). Moreover, the CBR of the BP_{ND}s was considerably larger than the fluorescence uptake: 47.2±14.7, 39.5±6.2, 23.3±4.6, 7.5±3.5, and 3.8±0.8 for the A431, AsPC-1, U251, 9L-GFP, and blocked U251, respectively. The non-zero CBR of the blocked U251 suggests either that the blocking was incomplete or that there are slight differences in either non-specific binding or the plasma input curve between the two reporters. However, the excellent

correlation between *in vivo* and *in vitro* binding potentials suggests that whatever the reason, it does not seem to affect the quantitative potential of the approach. Further studies are on going using fluorescently labeled, targeted, and untargeted affibodies to employ reporters that are more chemically similar.

Fig. 5a demonstrates the validation of the dual-reporter BP_{ND} measurements against *ex vivo* measures of binding potential from tissue slices. A very strong linear correlation was observed (r=0.99, p<0.01) with a slope of 1.80±0.48 and an intercept of −0.58±0.84. Some mismatch between the *in vivo* and *ex vivo* binding potentials were expected since the *ex vivo* measurement was based on the assumption that the blood concentration was negligible (leading to a possible underestimation of the *ex vivo* BP_{ND}). Furthermore, it was not possible to remove the effect of autofluorescence in the *ex vivo* images, which was more pronounced for the untargeted images (leading to the possible overestimation in the slope).

The BP_{ND} measurements also correlated well with the *in vitro* BP measurements (from flow cytometry and histology) for the 9L-GFP, U251, and AsPC-1 tumor groups (Fig. 5b), but not for the A431, which displayed a very high expression of EGFR *in vitro*. For comparison purposes, the average binding potential measured *in vivo, ex vivo*, and *in vitro* for all tumor lines, as well as the average flow cytometry measures of receptor density per cell and the histological measures of cell density, are displayed in Table 1.

The discrepancy between *in vivo* and *in vitro* measures of EGFR expression in the A431 tumor line was also observed by Aerts *et al.* [23], and McLarty *et al.* demonstrated that *in vitro* measures of receptor density in tumor lines that express abnormally high levels of HER2 receptor severely overestimate the *in vivo* measured binding potential [24]. These results highlight a potential pitfall in using *in vitro* measures to predict *in vivo* receptor expression characteristics. That is, *in vitro* measures determine the total number of receptors, and *in vivo* measures presumably determine the total amount of receptors *available for binding* [16]; therefore, if the *in vivo* structure or biology of a tumor inhibit a significant fraction of binding to receptors, *in vitro* measures can grossly overestimate the *in vivo* receptor availability. A number of factors can influence the total number of receptors available for binding *in vivo, e.g.*, the binding site barrier effect [25] and high inter-tumoral pressure [26], which impair the ability of a reporter to diffuse far from blood vessels.

While the results of this study highlight the potential of the dual-reporter approach to quantify receptor expression *in vivo*, there are some potential limitations that require further study. First, the model requires that other than the ability of the targeted reporter to bind to a specific receptor, the untargeted and targeted reporters have identical pharmacokinetics. In this study, a somewhat arbitrary untargeted reporter was used that was found to have a similar plasma uptake curve to the targeted reporter [15], to display a similar uptake curve to the targeted reporter in the blocking study (Fig. 2a). However, in the future, it may be preferable to use an enantiomer of the targeted reporter to minimize any differences between the reporters. For example, for EGFR targeting, it would be possible to use an anti-EGFR Affibody® imaging agent for the targeted reporter and a negative control Affibody® imaging agent for the untargeted reporter [27]. Second, even if the targeted and untargeted reporters are otherwise identical, the model also relies on the assumption that the system has reached a steady state and that the bound and free states of the targeted reporter are in an instantaneous equilibrium. The validity of these assumptions was superficially tested by a full kinetic model using approximate kinetic parameter inputs: less than a 4% error in the dual-reporter model-measured binding potential was found (results not shown). However, further simulation studies are ongoing to fully characterize the sensitivity of the dual-reporter to all model assumptions: *e.g.*, the affect of discrepancies between the two reporters in terms of plasma kinetics and non-specific binding, the affect of cellular internalization,

and the affect of reporter affinity (*i.e.*, how reversible or irreversible the targeted reporter binding is to its receptor). Finally, in this study, the fluorescence of the untargeted and targeted reporters was measured at considerably different wavelengths (700 and 800 nm, respectively). Therefore, due to potential differences in tissue light absorption and scattering properties at these two wavelengths, it is possible that the detection sensitivity volume profiles of the two reporters could differ. Further investigation is necessary to fully elucidate the potential magnitude of this effect and to determine the affect this discrepancy could have on the modeling; however, it is known that the optical properties of tissue at these two wavelengths are relatively similar [28], and the epi-illumination geometry of the imaging system used makes the images at both wavelengths particularly surface weighted, exemplified by the spatial resolution in Fig. 1b, c in which small blood vessels can be discriminated.

In conclusion, this is a report and validation of a novel, quick, and robust *in vivo* methodology for measuring receptor expression in tumors. There are several significant and widespread implications of this approach. For preclinical work, the approach could help guide drug discovery and development by providing an *in vivo* estimate of receptor expression before and after treatment to better analyze the efficacy of proposed therapeutics. The approach can also be applied clinically for cancer staging to stratify patients for treatment or to monitor therapy using an optical fiber probe in conjunction with tissue biopsy or using non-invasive imaging modality like single photon emission tomography that is capable of dual-reporter imaging on a human scale.

Acknowledgments

This research was funded by NIH grants P01CA84201, R01CA109558, and R01CA156177. K. M. T. was funded in part by a CIHR postdoctoral fellowship.

References

1. Weissleder R, Pittet MJ. Imaging in the era of molecular oncology. Nature. 2008; 452:580–589. [PubMed: 18385732]
2. Peer D, Karp JM, Hong S, Farokhzad OC, Margalit R, Langer R. Nanocarriers as an emerging platform for cancer therapy. Nat Nanotechnol. 2007; 2:751–760. [PubMed: 18654426]
3. Ntziachristos V, Tung CH, Bremer C, Weissleder R. Fluorescence molecular tomography resolves protease activity *in vivo*. Nat Med. 2002; 8:757–760. [PubMed: 12091907]
4. Weissleder R, Tung CH, Mahmood U, Bogdanov A Jr. *In vivo* imaging of tumors with protease-activated near-infrared fluorescent probes. Nat Biotechnol. 1999; 17:375–378. [PubMed: 10207887]
5. Chernomordik V, Hassan M, Lee SB, Zielinski R, Gandjbakhche A, Capala J. Quantitative analysis of Her2 receptor expression *in vivo* by near-infrared optical imaging. Mol Imaging. 2010; 9:192–200. [PubMed: 20643022]
6. Mintun MA, Raichle ME, Kilbourn MR, Wooten GF, Welch MJ. A quantitative model for the *in vivo* assessment of drug binding sites with positron emission tomography. Ann Neurol. 1984; 15:217–227. [PubMed: 6609679]
7. Lammertsma AA, Hume SP. Simplified reference tissue model for PET receptor studies. Neuroimage. 1996; 4:153–158. [PubMed: 9345505]
8. Logan J, Fowler JS, Volkow ND, Wang GJ, Ding YS, Alexoff DL. Distribution volume ratios without blood sampling from graphical analysis of PET data. J Cereb Blood Flow Metab. 1996; 16:834–840. [PubMed: 8784228]
9. Carmeliet P, Jain RK. Angiogenesis in cancer and other diseases. Nature. 2000; 407:249–257. [PubMed: 11001068]
10. Maeda H, Wu J, Sawa T, Matsumura Y, Hori K. Tumor vascular permeability and the EPR effect in macromolecular therapeutics: a review. J Control Release. 2000; 65:271–284. [PubMed: 10699287]

11. Goldenberg DM, Kim EE, DeLand FH, Bennett S, Primus FJ. Radioimmunodetection of cancer with radioactive antibodies to carcinoembryonic antigen. Cancer Res. 1980; 40:2984–2992. [PubMed: 7397693]
12. Hine KR, Bradwell AR, Reeder TA, Drolc Z, Dykes PW. Radioimmunodetection of gastrointestinal neoplasms with antibodies to carcinoembryonic antigen. Cancer Res. 1980; 40:2993–2996. [PubMed: 7397694]
13. Pogue BW, Samkoe KS, Hextrum S, et al. Imaging targeted-agent binding *in vivo* with two probes. J Biomed Opt. 2010; 15:030513. [PubMed: 20614996]
14. Liu JT, Helms MW, Mandella MJ, Crawford JM, Kino GS, Contag CH. Quantifying cell-surface biomarker expression in thick tissues with ratiometric three-dimensional microscopy. Biophys J. 2009; 96:2405–2414. [PubMed: 19289065]
15. Samkoe KS, Sexton K, Tichauer KM, et al. High vascular delivery of EGF, but low receptor binding rate is observed in AsPC-1 tumors as compared to normal pancreas. Mol Imaging Biol. 2011
16. Innis RB, Cunningham VJ, Delforge J, et al. Consensus nomenclature for *in vivo* imaging of reversibly binding radioligands. J Cereb Blood Flow Metab. 2007; 27:1533–1539. [PubMed: 17519979]
17. Samkoe KS, Chen A, Rizvi I, et al. Imaging tumor variation in response to photodynamic therapy in pancreatic cancer xenograft models. Int J Radiat Oncol Biol Phys. 2010; 76:251–259. [PubMed: 20005458]
18. Wikstrand CJ, McLendon RE, Friedman AH, Bigner DD. Cell surface localization and density of the tumor-associated variant of the epidermal growth factor receptor, EGFRvIII. Cancer Res. 1997; 57:4130–4140. [PubMed: 9307304]
19. Gibbs-Strauss SL, Samkoe KS, O'Hara JA, et al. Detecting epidermal growth factor receptor tumor activity *in vivo* during cetuximab therapy of murine gliomas. Acad Radiol. 2010; 17:7–17. [PubMed: 19796971]
20. Smith JJ, Derynck R, Korc M. Production of transforming growth factor alpha in human pancreatic cancer cells: evidence for a superagonist autocrine cycle. Proc Natl Acad Sci USA. 1987; 84:7567–7570. [PubMed: 3499610]
21. Gunn RN, Lammertsma AA, Hume SP, Cunningham VJ. Parametric imaging of ligand-receptor binding in PET using a simplified reference region model. Neuroimage. 1997; 6:279–287. [PubMed: 9417971]
22. Baselga J, Pfister D, Cooper MR, et al. Phase I studies of anti-epidermal growth factor receptor chimeric antibody C225 alone and in combination with cisplatin. J Clin Oncol. 2000; 18:904–914. [PubMed: 10673534]
23. Aerts HJ, Dubois L, Perk L, et al. Disparity between *in vivo* EGFR expression and 89Zr-labeled cetuximab uptake assessed with PET. J Nucl Med. 2009; 50:123–131. [PubMed: 19091906]
24. McLarty K, Cornelissen B, Scollard DA, Done SJ, Chun K, Reilly RM. Associations between the uptake of 111In-DTPA-trastuzumab, HER2 density and response to trastuzumab (Herceptin) in athymic mice bearing subcutaneous human tumour xenografts. Eur J Nucl Med Mol Imaging. 2009; 36:81–93. [PubMed: 18712381]
25. Fujimori K, Covell DG, Fletcher JE, Weinstein JN. A modeling analysis of monoclonal antibody percolation through tumors: a binding-site barrier. J Nucl Med. 1990; 31:1191–1198. [PubMed: 2362198]
26. Jain RK, Baxter LT. Mechanisms of heterogeneous distribution of monoclonal antibodies and other macromolecules in tumors: significance of elevated interstitial pressure. Cancer Res. 1988; 48:7022–7032. [PubMed: 3191477]
27. Tolmachev V, Rosik D, Wallberg H, et al. Imaging of EGFR expression in murine xenografts using site-specifically labelled anti-EGFR 111In-DOTA-Z EGFR:2377 affibody molecule: aspect of the injected tracer amount. Eur J Nucl Med Mol Imaging. 2010; 37:613–622. [PubMed: 19838701]
28. Franceschini MA, Gratton E, Hueber D, Fantini S. Near-infrared absorption and scattering spectra of tissues *in vivo*. In Proceedings of SPIE. 1999

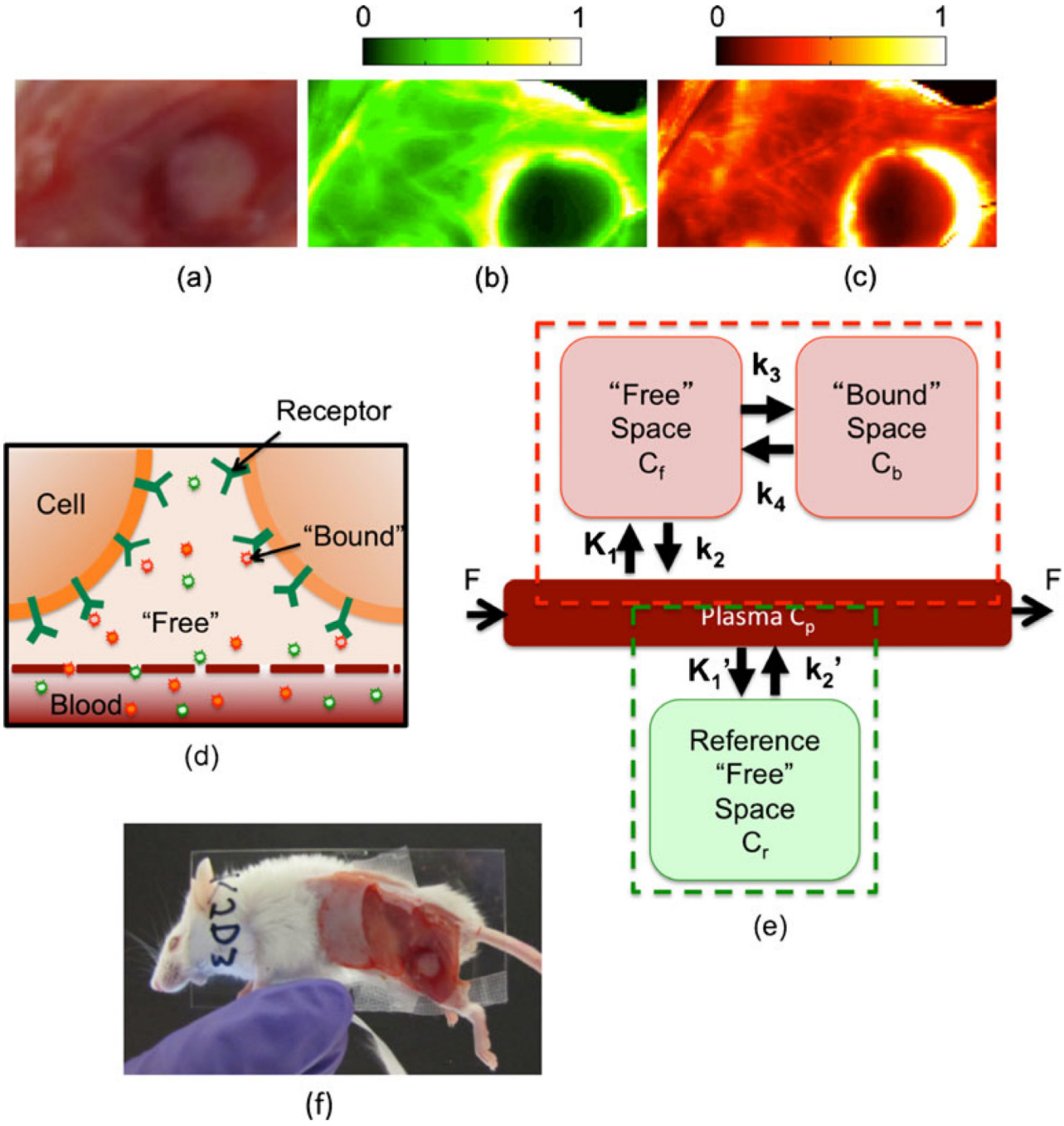

Fig. 1.

Compartment model for dual-reporter approach for determining receptor status *in vivo*. An example of some raw experimental results—specifically, the white-light image of a subcutaneous A431 tumor, the uptake of the untargeted reporter, and the uptake of the targeted reporter—is depicted in **a–c**, respectively. The units of fluorescence are arbitrary, and the scale is equivalent for both the targeted and untargeted fluorescence maps. An illustration of the presumed distribution of both targeted and untargeted reporter concentrations within the tissue is presented in **d**. Specifically, it is assumed that the untargeted reporter (*green*) is dispersed throughout the blood compartment and the

extravascular, intercellular (“free”) space, and that the targeted reporter (*red*) is dispersed throughout the blood, free, and “bound” space (*i.e.*, attached to the specific receptor). The compartment model associated with the distribution of the untargeted reporter (the *green dashed box*) and the compartment model associated with the distribution of the targeted reporter (the *red dashed box*) are presented in **e**. A picture of the mouse slide setup for imaging is presented in **f**.

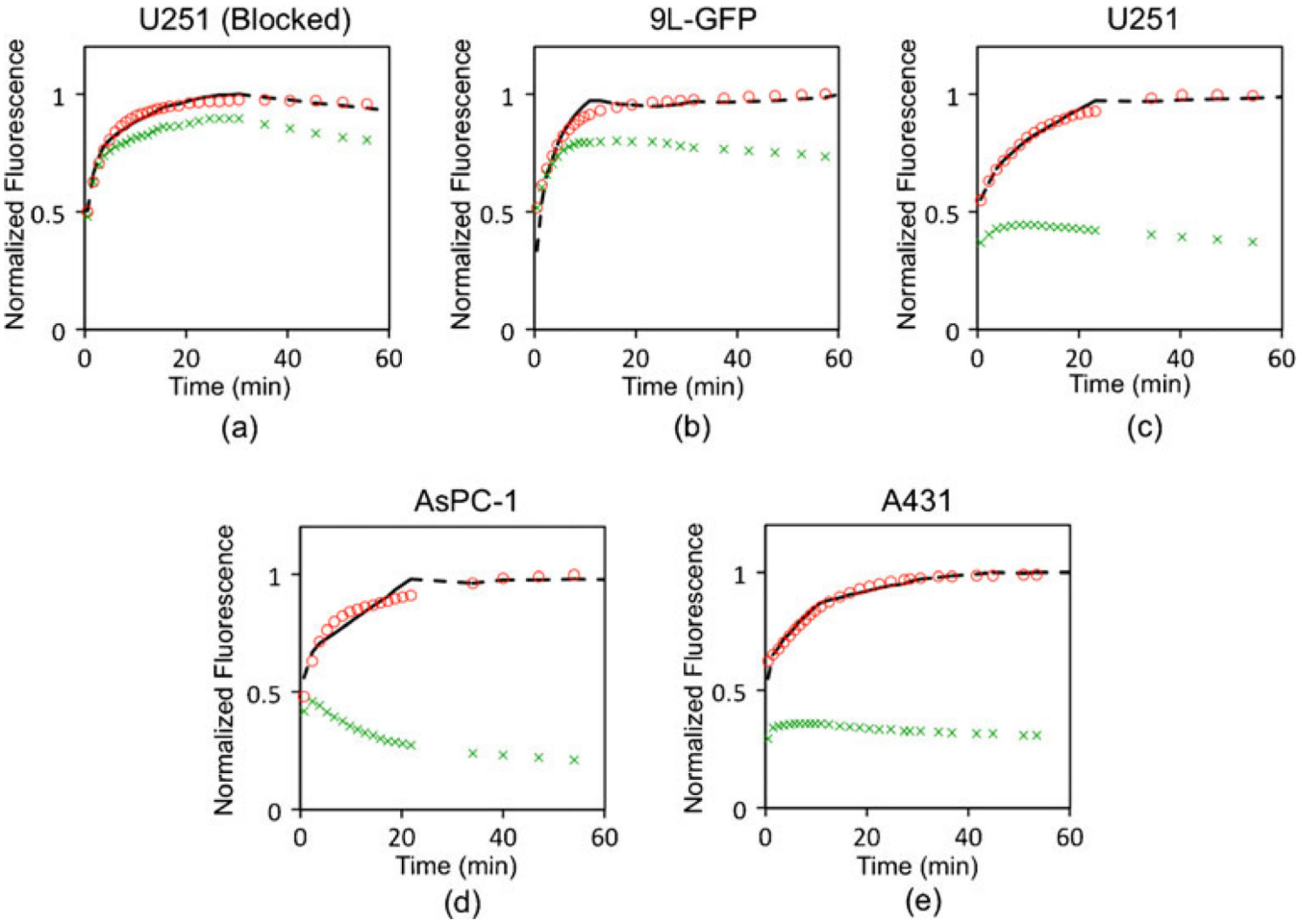

Fig. 2.

Targeted and untargeted reporter uptake. Typical fluorescence uptake curves of targeted (*red circles*) and untargeted (*green* "*x*"s") reporter over time (in minutes) in blocked U251, 9L-GFP, U251, AsPC-1, and A431 tumors are presented in **a–e**, respectively. These curves correspond to the specific tumors maps displayed in Fig. 3. The fluorescence in these curves is normalized to the maximum fluorescence in the targeted reporter within the 60-min window. The *black dashed line* in each subfigure displays the fit of the targeted reporter uptake curve using the dual-reporter model.

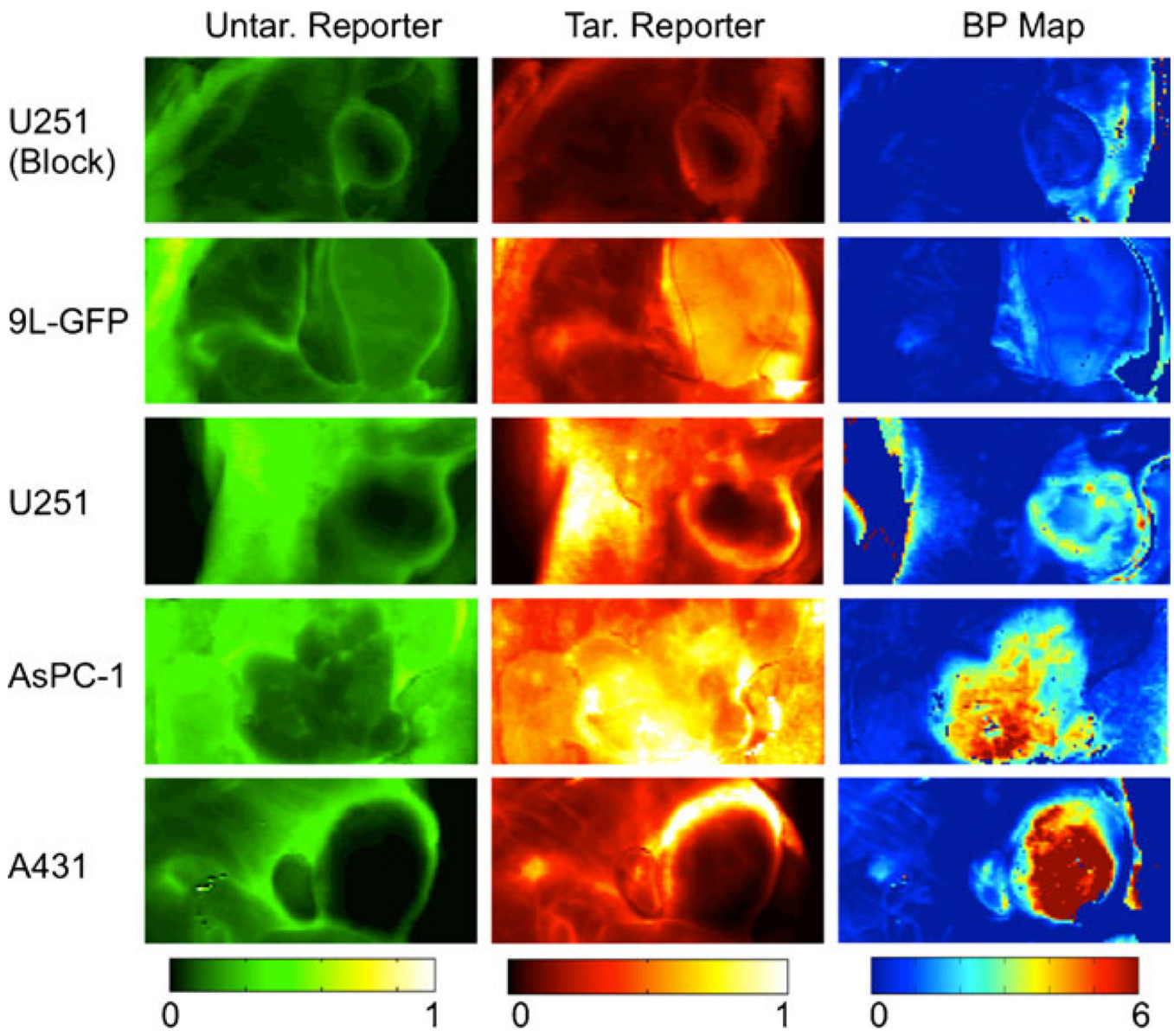

Fig. 3.

Binding potential maps. The tumor lines (*i.e.*, the *rows of the table*) were ordered to represent the expected levels of epidermal growth factor receptor availability, with availability increasing from the *top* to the *bottom*. The *first column* displays typical fluorescence uptake of the untargeted (Untar.) reporter in tissue including and surrounding each tumor line examined. The *second column* displays the uptake of the epidermal growth factor-tagged targeted (Tar.) reporter in the same tumors. These *images in the first two columns* were taken at 700 and 800 nm, respectively, using the LI-COR Odyssey scanner at 60 min post-reporter injection. The units of fluorescence are arbitrary, and the scale is equivalent for both the targeted and untargeted fluorescence maps. The *third column* presents the binding potential (BP) maps of the corresponding tumors in the *first two columns*. These were calculated using the Logan graphical adaptation of the dual-reporter model. Binding potential is a unitless value proportional to receptor expression.

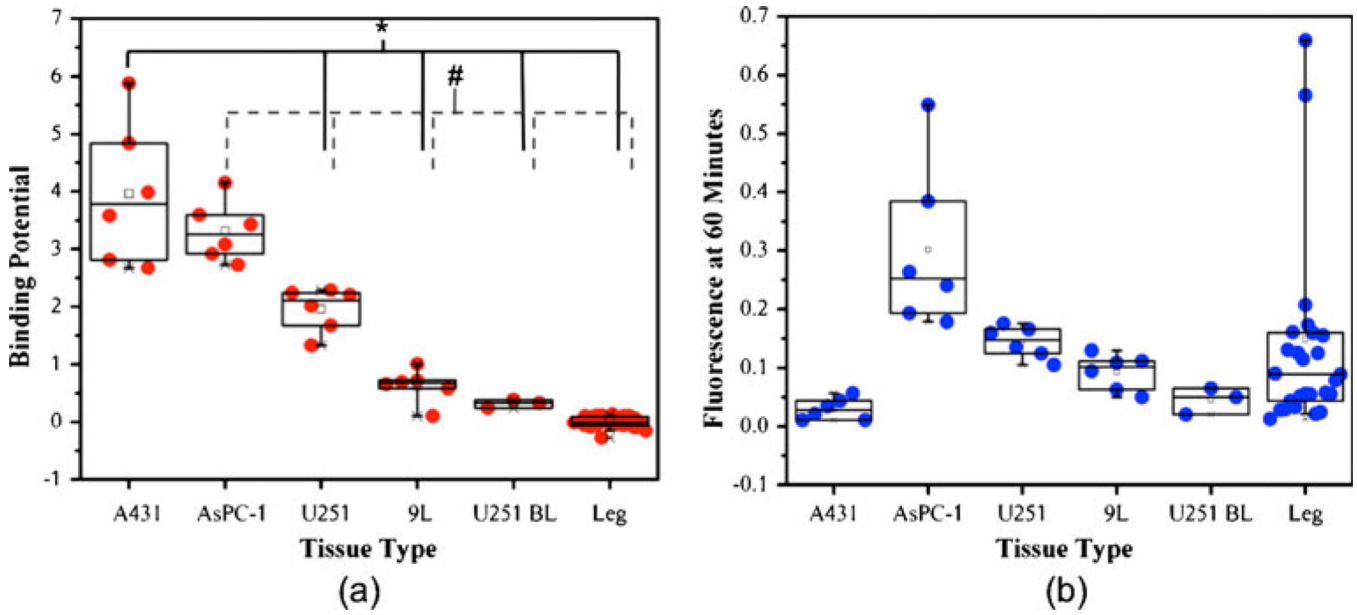

Fig. 4.

Binding potential vs. targeted reporter uptake. In **a**, a boxplot of the binding potentials (BP) calculated from the average targeted and untargeted reporter uptake curves in each tumor is presented against tumor line in descending order of expected epidermal growth factor receptor expression ($^{*}p<0.05$, $^{\#}p<0.05$). As a comparison, **b** displays the corresponding box plot of targeted fluorescence reporter uptake in each tumor at 60 min post-reporter injection.

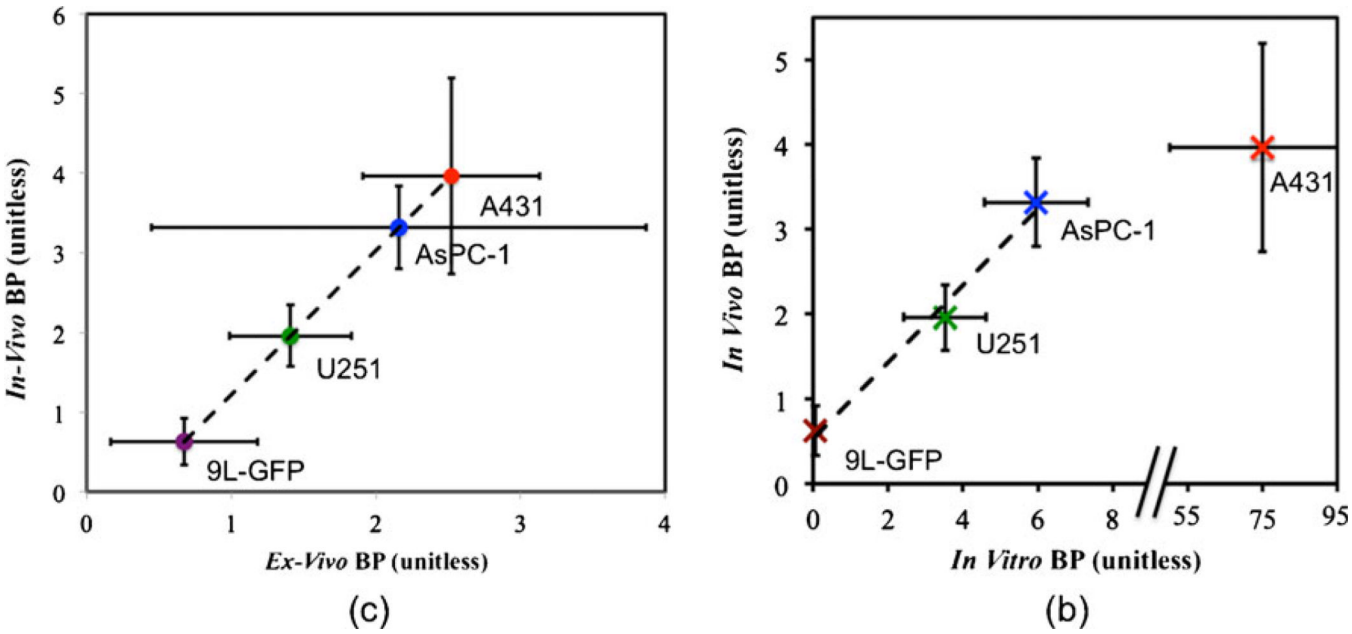

Fig. 5.

Validation of *in vivo* binding potential. In **a**, the correlation of the average *in vivo* BP of the 9L-GFP (*purple*), U251 (*green*), AsPC-1 (*blue*), and A431 (*red*) tumor groups to the corresponding *ex vivo* measured ratio of targeted to untargeted fluorescence from 10-μm tissue slices compared (r=0.99, p<0.01, slope=1.80±0.48, intercept=−0.58±0.84). In **b**, the correlation between *in vivo* BP and *in vitro* BP (measured from flow cytometry and histology) is displayed. The tumor groups are colored as in **c** with a significant correlation being observed for the 9L-GFP, U251, and AsPC-1 groups (r=0.99, p<0.01, slope= 0.64±0.32, intercept=0.47±0.51).

Table 1

The average *in vivo, ex vivo*, and *in vitro* binding potentials for each tumor line, in addition to the average number of receptors per cell measured by flow cytometry and average *in vivo* cell density measured by histology.

Tumor line	BP *in vivo* (unitless)	BP *ex vivo* (unitless)	BP *in vitro* (unitless)	Flow cytometry (EGFR/cell×10^5)	Cell density (cells/mm^3×10^4)
A431	3.96±1.23	2.52±0.61	75.80±22.03	12.00±2.42	3.80±0.80
AsPC-1	3.32±0.52	2.16±1.31	5.96±1.38	0.72±0.11	4.95±0.86
U251	1.96±0.38	1.41±0.42	3.52±1.10	0.44±0.11	4.85±0.95
9L	0.63±0.29	0.67±0.51	0.06±0.14	0.01±0.02	3.80±0.80

All values are presented as mean±SD